STEWARD-1040
Fermilab Library
0 1160 0007284 7

25

PREPRINTS

of the

STEWARD OBSERVATORY

MAR 2 1992

THE UNIVERSITY OF ARIZONA
TUCSON, ARIZONA 85721 U.S.A.

No ADS
No HEP

ROUTE TO
NAME | LOCATION

No. 1040

ADAPTIVE OPTICS FOR ARRAY TELESCOPES USING PISTON AND TILT WAVEFRONT SENSING[1]

P. Wizinowich, B. McLeod, M. Lloyd-Hart, J. R. P. Angel,
D. Colucci, R. Dekany, D. McCarthy, D. Wittman and I. Scott-Fleming

[1]Observations reported here were obtained at the Multiple Mirror Telescope Observatory, a joint facility of the Smithsonian Institution and the University of Arizona.

I. Scott-Fleming is with the Multiple Mirror Telescope Observatory, University of Arizona, Tucson, Arizona 85721. P. Wizinowich is now with the W. M. Keck Observatory, P.O. Box 220, Kamulea, Hawaii, 96743. He was formerly with the other authors at Steward Observatory, University of Arizona, Tucson, Arizona 85721.

Accepted for publication in Applied Optics.

Adaptive Optics for Array Telescopes using Piston and Tilt Wavefront Sensing[1]

P. Wizinowich, B. McLeod, M. Lloyd-Hart, J. R. P. Angel,
D. Colucci, R. Dekany, D. McCarthy, D. Wittman and I. Scott-Fleming

ABSTRACT

A near-infrared adaptive optics system, operating at ≈ 50 Hz, has been used to adaptively control phase errors between two mirrors of the Multiple Mirror Telescope by stabilizing the position of the interference fringe in the combined unresolved far-field image. The resultant integrated images have angular resolutions of better than 0.1 arcseconds and fringe contrasts > 0.6. Measurements of wavefront tilt have confirmed the wavelength independence of image motion. These results show that interferometric sensing of phase errors, when combined with a system for sensing the wavefront tilt of the individual telescopes, will provide a means of achieving a stable diffraction-limited focus with segmented telescopes or arrays of telescopes.

Key Words: adaptive optics, astronomy, stellar interferometry, telescopes, wavefront sensing.

Accepted for publication in Applied Optics.

[1] Observations reported here were obtained at the Multiple Mirror Telescope Observatory, a joint facility of the Smithsonian Institution and the University of Arizona.

I. Scott-Fleming is with the Multiple Mirror Telescope Observatory, University of Arizona, Tucson, AZ 85721. P. Wizinowich is now with the W. M. Keck Observatory, P.O. Box 220, Kamulea, HI, 96743. He was formerly with the other authors at Steward Observatory, University of Arizona, Tucson, AZ 85721.

1. INTRODUCTION

An adaptive optics system has been constructed for the Multiple Mirror Telescope (MMT), for operation in the 1 to 3.5 μm wavelength range, and we have begun real-time tests of its performance at the telescope.[1] The MMT consists of six co-mounted 1.83 m diameter telescopes, arranged in a hexagonal pattern on a 2.52 m radius circle, as shown in figure 1. The telescopes are routinely operated in a coherently phased mode where the optical path difference between telescopes is less than the coherence length for the observed spectral band.[2] With an overall baseline of 6.86 m, the MMT thereby offers the highest potential diffraction-limited angular resolution of any existing optical telescope. While atmospheric turbulence blurs the integrated image, at near-infrared wavelengths the instantaneous image from a single 1.8 m telescope is near diffraction-limited. Adaptive correction of the atmospherically induced wavefront tilt and piston for each telescope is sufficient to achieve an integrated image at the combined focus of all six telescopes with the diffraction-limited resolution of the full MMT.[3] The optical path difference (OPD) between telescopes can be determined from the interference fringes in the image of a star produced by a pair of telescopes. We report here on the use of a pair of adaptive segments to control the piston errors between two MMT telescopes by stabilizing the brightest interference fringe, a process we refer to as adaptive phasing.

One method we are developing for wavefront sensing for array telescopes uses neural networks to determine the relative tilt and piston of each telescope.[3] The purpose of the adaptive phasing, and tilt sensing, experiments described in this paper was to begin exploring an alternate approach in which the tilt of each aperture is measured with an individual tilt sensor and the piston difference between pairs of telescopes is determined from the phase of the two beam interference. The potential advantage of such a tilt and piston wavefront sensor is one of signal-to-noise based on the fact that fewer detector elements are required. A reduced detector readout noise contribution allows fainter reference stars to be used for wavefront sensing. The neural network approach is still extremely valuable however since it evaluates the combined image or final product of the adaptive system. We therefore plan to implement both techniques in the MMT adaptive instrument.

Fringe tracking and tilt sensing are routinely used in astronomical interferometers to compensate for path length fluctuations and to keep the two beams parallel. The term adaptive phasing has been used in this paper, instead of fringe tracking, to point out the differences between the two techniques and to emphasize the goal of this correction. The Mark III stellar interferometer performs fringe tracking by determining the phase from the detected signal in the pupil plane as the path length is modulated over one fringe.[4] Since the fringes are not directly imaged the high resolution information must be reconstructed from the measured fringe contrast and position. In contrast, our technique allows us to obtain directly high resolution images, and to perform long integrations on the detector array, since the fringe position in the image plane is locked, not modulated, by the servo loop. We are using the MMT as an imaging interferometer. The goal of our approach is to use adaptive optics to compensate for the atmospherically induced piston errors between

all pairs of telescopes so that high resolution images can then be obtained of faint objects within the isoplanatic patch of the star used for wavefront sensing (This patch is substantially smaller than the instrumental isoplanicity of the MMT.[2]).

The remainder of this paper is broken into four sections beginning with a brief review of two beam interference and the impact of atmospheric turbulence on image quality. This is followed by descriptions of the adaptive optics system, the adaptive phasing procedure and an experiment to measure simultaneously wavefront tilt at visible and infrared wavelengths. The observations are then presented and evaluated. Before concluding we discuss how the technique can be improved and present some thoughts on the simultaneous adaptive phasing of all six telescopes using tilt and piston wavefront sensing.

2. THEORETICAL BACKGROUND

2.1 Two Beam Interference

In the absence of atmospheric turbulence, the diffraction-limited images of a single star produced by an array of telescopes can be stacked directly on top of each other. An overall tilt of the wavefront will simply shift the position of this combined image, while tilts between telescopes will cause the images to become unstacked. As the OPD or piston between the telescopes is reduced interference fringes will begin to appear. When a pair of telescopes is perfectly phased, or when the OPD is equal to an integer number of waves for monochromatic operation, a bright fringe will be centered on the combined image. Piston changes between the telescopes, which have no effect on the combined incoherent image, will cause the bright fringe to move with respect to the energy center of the image.

If the light from two identical unaberrated uniformly-illuminated circular apertures is perfectly superposed the signal at any point in the image will simply be double that for a single aperture, providing there is no coherence. If there is perfect coherence between the two beams, $I_a(\alpha_x,\alpha_y)$ and $I_b(\alpha_x,\alpha_y)$, then the resultant intensity distribution is given by the equation for two beam interference,

$$\begin{aligned} I(\alpha_x,\alpha_y) &= I_a + I_b + 2\sqrt{I_a I_b}\cos\phi \\ &= 2I_a(1+\cos\phi) \qquad , \text{ if } I_a = I_b, \end{aligned} \tag{1}$$

where α is the angle between the observation point and the center of the diffraction pattern, and $\phi(\alpha_x,\alpha_y)$ is the phase difference between the beams.[5,6] For the no aberration case with zero OPD, $\phi = (2\pi/\lambda)(\alpha_x D_x + \alpha_y D_y)$, where D is the center to center separation of the two mirrors, implying a fringe spacing of λ/D and a full width at half maximum (FWHM) of $\lambda/2D$.

Figure 2(a) is an intensity profile, perpendicular to the fringes, of the incoherent and coherent diffraction-limited intensity distributions for two MMT mirrors of diameter d = 1.83 m, with a center-to-center azimuthal separation (see figure 1) of D = 4.36 m, at a wavelength

of $\lambda = 2.2\ \mu m$. The two images were assumed to be perfectly costacked (ie. no differential tilt between the apertures) and cophased (zero OPD). The FWHM for the coherent and incoherent cases are 0.051 and 0.255 arcsec, respectively. The effect of a π phase error on the costacked, coherent image is shown in figure 2(b). As the images become unstacked, figure 2(c), the fringe peaks will decrease and, since there is only a single line along which $I_a = I_b$, the fringe minima will not in general go to zero.

2.2 Atmospheric Turbulence

The following equations relate the image and wavefront to atmospheric turbulence and are useful in evaluating the performance and requirements of the adaptive system. According to Fried[7] and Noll[8] the mean square phase error, or variance, of the wavefront for Kolmogorov atmospheric turbulence before and after the removal of the mean wavefront tilt is

$$\sigma_1^2 = 1.030\ (d/r_0)^{5/3} \text{ and} \qquad (2a)$$
$$\sigma_3^2 = 0.134\ (d/r_0)^{5/3}\ , \qquad (2b)$$

respectively, where d is the aperture diameter and r_0 is the coherence length. For a single telescope the tilt contribution, $\sigma_T^2 = \sigma_1^2 - \sigma_3^2$, can be directly related to the observed root mean square image motion, α_{rms},

$$\sigma_T^2 = [(2\pi/\lambda)(\alpha_{rms} d/4)]^2\ . \qquad (3)$$

The overall tilt of the wavefront introduces a piston error, ϕ_P, between telescopes, given by the structure function for Kolmogorov turbulence,[7]

$$\phi_P = 2.62\ (D/r_0)^{5/6}\ , \qquad (4)$$

where D is the center-to-center separation of the telescopes. For a near-monochromatic beam, a fringe maximum with reduced intensity will occur whenever the piston error is equal to an integer number of waves and is less than the coherence length. The average effective atmospheric piston error contribution is therefore $\pm\pi/2$.

For small phase errors ($\sigma^2 < 1\ rad^2$, global tilt removed), the Strehl ratio, the ratio of the peak intensity of an aberrated image to that of a perfect image, can be determined from the relation

$$SR = e^{-\sigma^2} \qquad (5)$$

Perfect tilt and piston correction for the six MMT telescopes under median seeing conditions, $r_0 = 1.03$ m, would result in a near diffraction-limited image with FWHM ≈

0.067 arcsec and a Strehl ratio of $\approx$ 0.7 at 2.2 μm wavelength.

2.3 Fringe Contrast

The fringe contrast or visibility of an image is defined here as

$$\gamma = \frac{I_{max} - I_{min}}{I_{max} + I_{min}} , \qquad (6)$$

where I_{max} and I_{min} represent the intensities at the maximum and first minimum of the interference pattern. This definition is slightly different from the one used in stellar interferometry where one can measure the contrast at one point by modulating the phase. Beckers has compiled a list and error budget for the factors which reduce fringe contrast.[9] The dominant factors which directly effect γ are the bandpass, $\pm\Delta\lambda$, of the filter, the atmospheric residual aberrations, given by equation 2(b), and any fixed optical aberrations in the two telescopes.

To determine the contrast reduction due to a finite bandpass we must average equation 1 over a range of wavelength. For a square bandpass this goes to

$$I = \frac{I_{max}}{2}\left[sinc\left(\phi\frac{\Delta\lambda}{\lambda}\right)\cos\phi + 1\right] . \qquad (7)$$

The first minimum occurs very close to $\phi=\pi$; there, I_{min} = 0.01 I_{max} or $\gamma=0.98$ for $\lambda=2.2\pm0.21$ μm. This is not a significant contribution.

We have estimated the fringe contrast reductions due to atmospheric and telescope aberrations via numerical simulations. We have generated 100 wavefronts distorted by Kolmogorov turbulence with r_0 = 1m. The wavefronts were propagated through a 2 telescope aperture and then each of the resulting monochromatic 2.2μm images is recentered on the brightest fringe. With no telescope aberrations this yields an integrated image with fringe contrast $\gamma=0.76$. If we add estimated telescope aberrations (primarily focus errors and distortion due to the three hardpoint supports of each primary), the contrast drops to 0.72 .

A final reduction in contrast is caused by the delay between taking an image and then adjusting the adaptive mirror to recenter the fringes. The result is a residual error in the position of the fringes in the individual images. If the RMS error in the fringe position is $\Delta\phi$, we can estimate from equation 1 that for an integrated image, $I_{max} \alpha 1 + \cos\Delta\phi$, and $I_{min} \alpha 1 + \cos(\pi+\Delta\phi)$, implying that $\gamma = \cos\Delta\phi$. We will show later that a typical residual phase error is $\Delta\phi$ = 0.4 radians, giving γ = 0.85. Multiplicatively combining all the contrast reductions together gives a prediction for a typical observed contrast of 0.60.

3. SYSTEM DESCRIPTION

3.1 Adaptive Optics System

Our adaptive optics system is discussed in detail elsewhere.[1] It can be briefly described as consisting of a six segment adaptive mirror on which the six MMT primaries are reimaged and an infrared camera located at the combined image plane of all six telescopes. The adaptive mirror was provided by Thermo Electron Technologies Corporation.[10] Each segment is mounted on a co-axial tube piezo-electric actuator with three electrodes at 120° separation and 10 μm of stroke. The three electrodes allow a single mirror to be tilted in any direction, with or without introducing an overall piston. The infrared camera is a 62×58 pixel InSb array.[11] Non-destructive reads of a sub-array can be performed at a rate of 18 μs/pixel pair.

3.2 Adaptive Phasing of Two Telescopes

The procedure for adaptive phasing begins with a non-destructive read of a fixed ≈20×20 pixel array in which the image is located. Figure 3 is a schematic of the timing diagram. The pixel values are copied from one part of memory to another and the pixel values for the previous image are subtracted. An algorithm, discussed below, is then used to determine the x and y coordinates of the image and these coordinates are shipped over a SCSI link to a PC where they are converted to the appropriate driving voltages for the adaptive mirror. The total time from the start of reading an image to setting the adaptive mirror is 12.7 ms.

For this experiment the x and y coordinates used to drive the two adaptive mirror segments were simply the coordinates of the brightest pixel within the central 6×6 pixel field. When applied to the image from a single telescope no piston, only tilt, was introduced. For a pair of telescopes the two adaptive segments were independently tilted and pistoned, as if they were part of a single steering mirror, to bring the brightest pixel to the center of the array. The process was therefore equivalent to autoguiding on the brightest pixel, not the energy centroid. The question of the optimal image criterion for phasing is discussed in section 5. The observations described in sections 4.1 to 4.3 were obtained at the MMT in June, 1991.

3.3 Measurements of Wavefront Tilt

A separate experiment from the one described above was performed at the MMT in January, 1991. The six MMT pupils were reimaged onto a wedge prism which separated the six stellar images onto a video rate Pulnix CCD camera. The camera was operated in a non-interlaced mode providing sequential 16.7 ms (60 Hz) exposures. Use of a beamsplitter also allowed images from the same telescopes to be recorded simultaneously on the IR

camera, described above, operating at a 30 Hz frame rate. The dual purpose of this experiment was to measure the speed and magnitude of the atmospherically induced wavefront tilt and to determine if there was any dependence on wavelength. The tilt of the wavefront was estimated by computing the centroid of each image. The results of this experiment are briefly discussed in section 4.4.

4. OBSERVATIONS

4.1 Integrated Images

Figure 4 is a series of integrated images, from the interference of two MMT telescopes, obtained with and without adaptive phasing/bright pixel tracking. These integrated images were made by directly co-adding 1000 flat-fielded frames of 100 Hz data. Each data set is continuous with the exception of a camera reset after every 5th frame, requiring 9.4 ms. A vertical, or horizontal, cut through the peak of the integrated images was made to obtain the plots on the right of figure 4. We shall refer to the four data sets, from top to bottom, as images I, II, III and IV, respectively. Image I is the integrated image from a single MMT telescope. With reference to figure 1, image II is the combined image from telescopes A and F, while images III and IV resulted from the interference of telescopes A and C. Images I and II were taken at a different plate scale than the last two. These observations were obtained on three different nights, only images III and IV were recorded on the same night. The first part of table 1 contains the parameters for these images: the star name, the filter wavelength, λ, and its bandpass, $\pm \Delta\lambda$; the center-to-center telescope separation, D; the predicted fringe separation, λ/D; and the plate scale used on the IR camera. The second part of the table contains measurements on the integrated images of figure 4.

The very good seeing conditions are reflected by the fact that there is some evidence of fringes even in the integrated image without tracking. Even this faint indication of fringes would however disappear in a longer exposure. The fringe contrast, as high as 0.66, in the fringe tracking case is quite impressive; we had predicted $\gamma = 0.6$, under median seeing conditions, in section 2.3. These estimates of fringe contrast were calculated using equation 6 and the intensities of the central peak and first minimum in the integrated image. The improvement in peak intensity is not as impressive as might have been hoped for the reasons discussed in section 4.3.

The fringe spacing of the corrected integrated images is 15 to 20% narrower than our simple predictions. This is accounted for by two factors. First, the fact that the sinusoidal interference pattern is multiplied by an Airy pattern mathematically causes the fringe maxima to be shifted toward the center of the Airy pattern by 7% (see figure 2(a)). The remainder is because the pupil mask in front of the adaptive mirror inadvertently blocked some of the light coming from the inner edge of each telescope.

4.2 Temporal Evolution of Phase

The temporal evolution of the phase difference between the two telescopes was measured by recording the position of the brightest pixel in the central 6×6 pixel field of each image frame. In order to track the absolute change in phase an offset ($\pm 2\pi$) was added each time the brightest pixel location changed by an amount equal to the fringe separation.

Figures 5(a) and (b) show the vertical fringe position, or phase, versus time for the uncorrected and corrected images, respectively, of data set III. The measured fringe separation for this data set was f = 4.5 pixels. The bright pixel location, in pixels, was therefore multiplied by $2\pi/f$ to convert to phase. Figure 5(c) is the result of directly integrating the fringe position shown in figure 5(b) and corresponds to the inverse of the integrated piston motion of the adaptive mirrors. Figures 5(a) and (c) represent the atmospherically induced change in the OPD between the two telescopes during the uncorrected and corrected integration times, respectively.

Figure 5 is limited by a one pixel resolution in measuring the fringe position. A more accurate measure of phase can be obtained by finding the phase of the cosine term which best fits all the data. This can be accomplished by maximizing the cosine fringe fitting coefficient

$$\beta = \sum_i I_i \cos\left(\frac{2\pi x_i}{f} - \phi\right) \qquad (8)$$

by varying the phase, ϕ, and fringe spacing, f. When ϕ and f are adjusted so that the cosine term is aligned with the intensity pattern, β will be at a maximum. I_i and x_i are the intensity and x coordinate of pixel i. Both x_i and f are measured perpendicular to the fringes in units of pixels. Figures 6(a) and (b) are equivalent to figures 5(a) and (b) with the improved resolution provided by maximizing β.

Equation 8 has been applied to the individual frames which were coadded to obtain images II, III and IV. The standard deviation and peak-to-peak variation of the determined phase, with and without adaptive phasing, are listed in the third part of table 1 and show the improvement with adaptive phasing. Equation 4 can be used to obtain an estimate of r_0 from the measured standard deviation of the uncorrected phase. This estimate is an upper limit since the 12 second integrations are too short to adequately sample the atmospherically induced piston variations. The calculated upper limits for r_0 are 2.9, 3.3 (or 1.5 m from figure 4(c)) and 2.9 m, at 2.2 μm wavelength, for images II, III and IV, respectively. These values are quite large, but the seeing was very good. A second estimate of r_0 can be obtained from the equation $r_0 \approx \lambda/\mathrm{FWHM}$ and the measured FWHMs of the uncorrected integrated images listed in table 1. These estimated r_0 values of 1.3, 1.8 and 1.4 m at 2.2 μm for images II, III and IV, respectively, are lower due to errors in costacking the two images which add to the measured FWHM. The FWHM of the single mirror image

I in figure 4, taken under poorer seeing conditions, corresponds to $r_0 \approx 0.9$ m.

In order to determine the required bandwidth for the piston correction system the change in phase as a function of time must be examined. For the uncorrected image II the average phase differences for measurements separated by 10 and 20 ms were 0.17 and 0.22 rad, respectively. The corresponding numbers for image III were larger, 0.27 and 0.40 rad, due to the increased separation of the telescopes and the $D^{5/6}$ dependence of the piston error as seen in equation 4. In the worst of these cases the mean square phase error increases by 0.16 rad^2 due to a 20 ms delay between piston sensing and correction. If this mean square error contribution were added to an initial error due to residual atmospheric or telescope aberrations, equation 5 would predict a 15 % reduction in the Strehl ratio. A 50 Hz piston correction rate therefore seems acceptable at least under these good seeing conditions.

4.3 Brightest Pixel versus Energy Centroid

The relationship between the brightest pixel and energy centroid in the individual image frames was studied to determine the effectiveness of our adaptive phasing technique. Clearly the technique can be substantially improved by making use of not only the phase information provided by the fringe position but also the wavefront slope information provided by the energy centroid.

Figure 7(a) is a plot of the intensity of the brightest pixel in the individual frames of the corrected image III as a function of the absolute value of the azimuthal difference between the position of the energy centroid and the position of this brightest pixel. Ideally the difference should be zero corresponding to zero OPD between the two telescopes. There is always a fringe within 0.5 fringes of the energy centroid which explains why the brightest pixel is nearly always within this range. Since the brightest pixel location is only measured to within a pixel, or 0.22 fringes, this upper limit is actually 0.6 fringes. The few low intensity data points occur when two or more fringes are near the same intensity level.

Figure 7(b) is the same plot as figure 7(a), but for the brightest pixel of the tracked fringe within the central 6×6 pixel field of each frame. The intensity of the brightest pixel of course decreases as the separation of the tracked fringe and energy centroid increases. The mean azimuthal separation of the energy centroid and tracked fringe is 0.043 arcsec, corresponding to a 23% decrease in the average brightest pixel intensity as indicated by the solid, least-squares fit, line in figure 7(b). This is what we actually did to obtain the corrected image III and shows the deficiency of the method.

The scatter, or rather reduction, in the bright pixel intensity at any one value of the bright-pixel/energy-centroid separation is primarily due to the atmospherically induced change in the relative tilts of the telescopes which causes the two images to become unstacked (see figure 2(c)). For example, the intensity of the brightest pixel is reduced by a factor of two, from the costacked and cophased case, when the two images (Airy patterns)

are separated by their FWHM ≈ 0.26 arcsec. This intensity reduction could be removed by having separate tilt sensors for each telescope. These sensors would also ensure that the energy centroid was always at the center of the image.

The variations in the intensity of the brightest and average pixels of the individual frames of the corrected images are listed in the last section of table 1. The average pixel intensity variation was also included to indicate the significance of atmospheric transmission variations and wavefront tilts large enough to drive the energy centroid too near the edge of the frame. Clearly this was a problem for image I (cirrus clouds), and somewhat of a problem for IV, but was not significant for images II or III.

Figure 8 provides a measure of the best possible performance of a system correcting the piston and tilt differences between a pair of telescopes. The plotted profiles are for the individual frames of the corrected images II and III with the maximum brightest pixel intensity. These images are close to the ideal case of no relative tilt or piston between the two telescopes. Figure 8(a) has a fringe contrast of 0.87 and represents a factor of 5 increase in peak intensity over figure 4(b).

4.4 IR versus Visible Tilt Sensing

Figure 9 is a plot of the infrared ($\lambda = 2.2\ \mu$m) image centroid versus the visible ($\lambda \approx 0.7\ \mu$m) centroid for a single MMT telescope in azimuth. The slope of the best fit line is unity to the 1% level. The rms and peak-to-peak differences between the two azimuth centroid measurements are 0.05 and 0.27 arcsec, respectively. The corresponding differences in the elevation direction are 0.03 and 0.16 arcsec. The rms and peak-to-peak single telescope azimuth or elevation image motion for 17 seconds of CCD data from this data set was 0.086 and 0.50 arcsec, respectively. Equations 3 and 2 can be used to obtain an estimated σ_T^2 = 0.59 rad^2 and r_0 = 2.3 m, at λ = 2.2 μm, from the measured rms motion. This corresponds to rather good seeing as evidenced by the observed Airy pattern, but is again an upper estimate of r_0 since the duration of the data set is probably insufficient.

The average change in atmospherically induced tilt for a single telescope, as measured by the image centroid position, was calculated from the above CCD data set to get an idea of the rate of change and temporal correlation. This data is plotted in figure 10. From this figure it can be seen that a delay of 16.7 ms between sensing and correcting the tilt results in an rms tilt error of α_{rms}=0.04 arcsec, corresponding to a mean square phase error contribution of σ_T^2 = 0.067 rad^2 from equation 3. A 50 Hz correction rate would therefore also seem to be quite reasonable for tilt.

5. DISCUSSION AND FUTURE IMPLEMENTATION

Energy centroiding on the combined image of a pair of telescopes is essentially equivalent to correcting for the average slope of the wavefront over the two telescope apertures. Adaptive phasing on an interference fringe between a pair of telescopes corrects

for the change in piston between the telescopes induced by the change in the overall tilt of the wavefront. It is not sufficient to track on the brightest fringe since which fringe is brightest will depend on which fringe is closest to the energy centroid, and would therefore result in jumping between fringes. This is the reason we made the field (6×6 pixels), for searching for the brightest pixel, less than one fringe in half width. Similarly it is even worse to track on the energy centroid since this will blur the fringes in the integrated, long exposure image. In order to maximize both the fringe intensity and contrast both the fringe position and the energy centroid must be used.

Note that the arguments about the difference between the energy centroid and the brightest fringe positions also hold for the combined image from all six MMT telescopes, and for that matter for the image from a large single aperture telescope. In this case the brightest fringe would be the brightest speckle in a short exposure image and its position is not necessarily coincident with the energy centroid. This is especially true as the number of speckles increases so that a single speckle is no longer dominant.

The optimal procedure which suggests itself for phasing two telescopes, given just the image plane information, is to globally tilt the adaptive mirror pair, as if they were a single mirror, on the energy centroid and then to piston them in opposite directions on the basis of the fringe position. Tilting the two mirrors as a single mirror implies that they are pistoned as well as tilted so that a piston term is not introduced between the adaptive mirrors. The OPD between the two telescopes could be equal to an integer number of wavelengths at this point. The white light fringe can be found by measuring the fringe contrast as the adaptive segments are used to change the OPD between the two telescopes in one wavelength steps (ie. jumping between fringes in the image plane).[4]

A smarter algorithm for fringe tracking than the brightest pixel position is required. An algorithm based on fitting equation 7 to the fringes would provide much more precise phase determinations. Tyson recommends using the fringe minima, instead of the maxima, since the Airy envelope has less effect on the position of the minima.[6]

A separate tilt sensor could be used to ensure that the images from each telescope remain costacked at all times. The fringe position would then only be required to provide information about the piston between telescopes. Piston sensing must be done near the wavelength of observation, unless the zero phase point corresponds to zero OPD; and in a rather narrow wavelength band for fringe contrast and coherence reasons. Tilt sensing, on the other hand, has two obvious advantages: it can be done with broadband visible light, permitting relatively low noise detectors, and it corrects for the relative tilts of the two apertures.

These techniques can be extended to work with more than two telescopes. For example, we intend to implement a small format, fast readout CCD camera with a wedge prism in front of it to separate all six images of the MMT. This is basically a Shack-Hartmann approach to wavefront sensing. However, the tilts cannot be unambiguously

integrated to obtain the entire wavefront due to the discontinuity of the wavefront data between segments. The piston errors between telescopes could be determined, for example, by independently interfering light from the six adjacent pairs of telescopes.

This leads to a discussion of the relative merits of piston sensing in the pupil and image planes. The critical issues are measurement accuracy and limiting magnitude of the reference star. It is not obvious which plane offers the highest accuracy and therefore the limiting magnitude, and its influence on accuracy, is perhaps more important. The dominant noise source is detector readout noise and since the detector technology will likely be the same in either plane then the selection should be based on minimizing the number of detectors and maximizing the system throughput.

For piston sensing in the image plane a linear array of at least six detector pixels would be required across the interference fringes for each telescope pair. A cylindrical lens could be used to compress the fringes onto the detector array. For the purpose of estimating a limiting magnitude, based on the stellar fluxes tabulated by Allen,[12] an integration time of 10 ms, a total system throughput of 25%, and a 10 electron read noise can be reasonably assumed. An average signal-to-noise ratio criterion per pixel of greater than three corresponds to a limiting K magnitude of ≈ 12.3.

6. CONCLUSION

An adaptive optics instrument, coupled with a simple adaptive phasing algorithm to track an interference fringe between two MMT telescopes, has been used to achieve integrated images with resolutions in one dimension of better than 0.1 arcsec. This resolution will be available for imaging substantially fainter objects within the isoplanatic patch around the star used for wavefront sensing. The success of this experiment has encouraged us to pursue a tilt and piston wavefront sensing approach to adaptive optics specially suited to segmented or array telescopes, where the wavefront is not continuous, but also applicable to single aperture telescopes. The proposed approach uses optical image centroids for sensing the tilt of the individual segments and infrared piston sensors, in the image or pupil plane, based on the interference between pairs of segments.

ACKNOWLEDGEMENTS

We would like to thank the technical staffs, particularly the late D. Young, of Steward Observatory and the MMT for their invaluable assistance; and A. Gleckler for useful comments on this paper. Financial support to develop the adaptive instrument was provided by the Flintridge Foundation and the director of Steward Observatory. Thermo Electron Technologies Corporation of San Diego provided the adaptive mirror. IR camera support is funded by NSF grant AST-8822465. McLeod acknowledges an NSF Graduate Research Fellowship. Dekany acknowledges support from the Jet Propulsion Laboratory.

REFERENCES

1. P. Wizinowich, M. Lloyd-Hart, B. McLeod, D. Colucci, R. Dekany, D. Wittman, R. Angel, D. McCarthy, B. Hulburd & D. Sandler, "Neural Network Adaptive Optics for the Multiple Mirror Telescope," SPIE Proc. **1542** (1991).
2. E. K. Hege, J. M. Beckers, P. A. Strittmatter & D. W. McCarthy, "Multiple Mirror Telescope as a Phased Array Telescope," Appl. Opt. **24**, 2565-2576 (1985).
3. J. R. P. Angel, P. Wizinowich, M. Lloyd-Hart & D. Sandler, "Adaptive Optics for Array Telescopes using Neural-Network Techniques," Nature **348**, 221-224 (1990).
4. M. Shao, M. M. Colavita, B. E. Hines, D. H. Staelin, D. J. Hutter, K. J. Johnston, D. Mozurkewich, R. S. Simon, J. L. Hershey, J. A. Hughes, & G. H. Kaplan, "The Mark III Stellar Interferometer," Astron. Astrophy. **193**, 357-371 (1988).
5. B. J. Thompson & E. Wolf, "Two-Beam Interference with Partially Coherent Light," JOSA **47**, 895-902 (1957).
6. R. K. Tyson, "Measuring Phase Errors of an Array or Segmented Mirror with a Single Far-Field Intensity Distribution," SPIE Proc. **1542** (1991).
7. D. L. Fried, "Statistics of a Geometric Representation of Wavefront Distortion," J. Opt. Soc. Am. **55**, 1427-1435 (1965).
8. R. J. Noll, "Zernike Polynomials and Atmospheric Turbulence," J. Opt. Soc. Am. **66**, 207-211 (1976).
9. J. M. Beckers, "The VLT Interferometer II. Factors Affecting On-Axis Operation," SPIE Proc. **1236**, 364-371 (1990).
10. B. Hulburd & D. Sandler, "Segmented Mirrors for Atmospheric Compensation," Opt. Eng. **29**, 1186-1190 (1990).
11. D. W. McCarthy, B. A. McLeod & D. Barlow, "An Infrared Array Camera for Interferometry with the Cophased Multiple Mirror Telescope," SPIE Proc. **1237**, 496-507 (1990).
12. C. W. Allen, Astrophysical Quantities, 3rd ed., 202 (Athlone, London, 1973).

Table 1. Observational parameters and data analysis for the integrated images of figure 4, including the measured variations for the individual (co-added) frames.

IMAGE	I	II	III	IV
Star Name	α Boo	κ Oph	β Cyg	β Cyg
$\lambda \pm \Delta\lambda$ (μm)	2.20±.21	2.26±.11	2.20±.21	1.64±.17
D (m)	0	2.52	4.36	4.36
λ/D (arcsec)	---	0.19	0.10	0.08
Plate scale (arcsec/pixel)	0.04	0.04	0.02	0.02
INTEGRATED IMAGE:				
Corrected Fringe Contrast	---	0.66	0.62	0.42
Corr. Fringe Spacing (arcsec)	---	0.15	0.085	0.065
Uncorr./Corr. FWHM (arcsec)	0.52/0.34	0.34/0.10	0.25/0.06	0.35/0.07
Ratio Corr. to Uncorr. Peak Intensity	1.27	1.96	1.34	1.82
PHASE OF UNCORRECTED/CORRECTED INDIVIDUAL FRAMES:				
Standard Deviation (rad)	---	2.28/0.57	3.32/0.60	4.87/1.08
Peak-to-Peak (rad)	---	10.5/4.52	15.4/4.90	22.2/7.31
INTENSITY OF CORRECTED INDIVIDUAL FRAMES:				
Brightest Pixel (arb. units):				
Mean ± Standard Deviation	1.74±0.81	13.05±2.5	1.32±0.16	7.09±1.9
Peak-to-Peak	4.34	14.65	0.96	10.85
Average Pixel (arb. units):				
Mean ± Standard Deviation	0.34±0.13	1.67±0.09	0.30±0.03	1.58±0.27
Peak-to-Peak	0.61	0.59	0.21	1.61

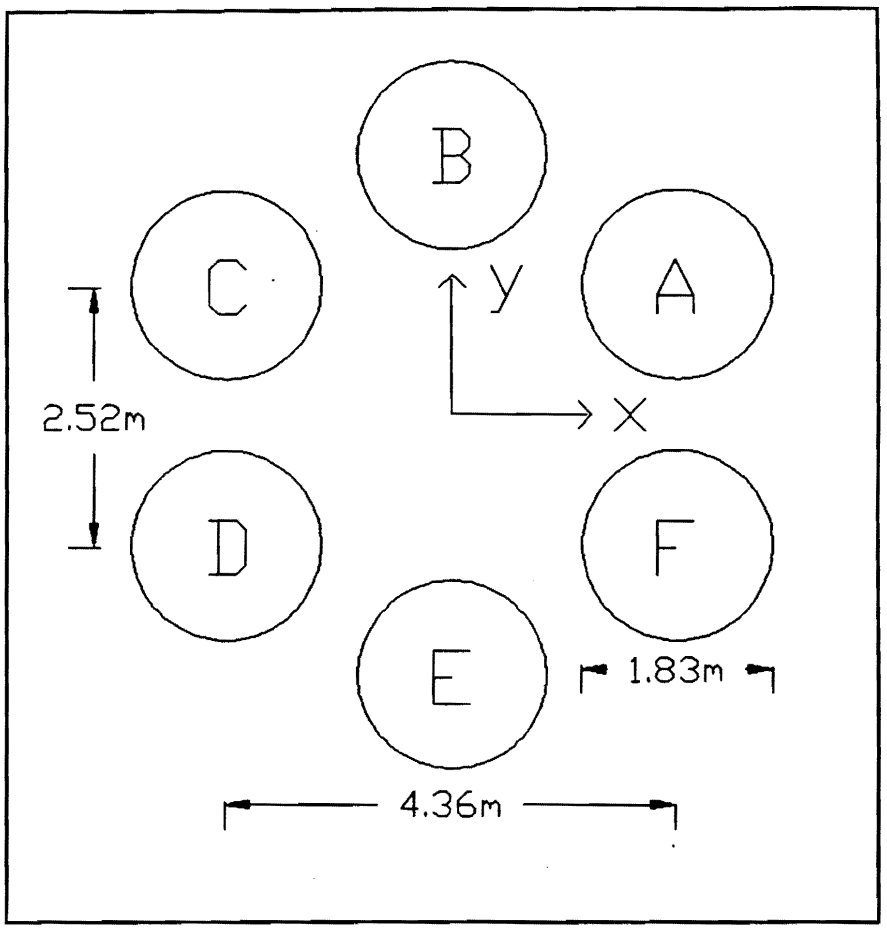

Figure 1. Configuration of the six MMT mirrors. The x and y directions correspond to the azimuth and elevation directions on the sky.

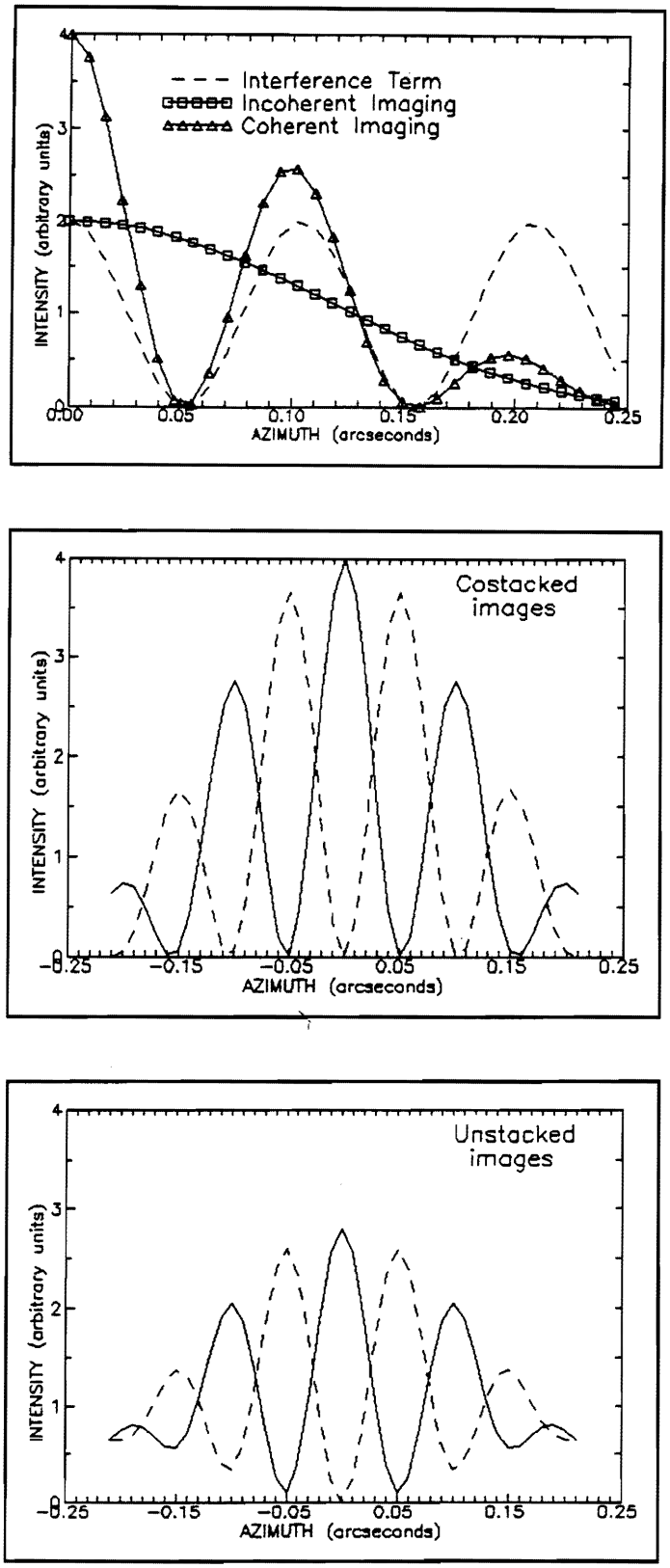

Figure 2. Simulated two beam interference intensity profiles for two MMT telescopes (A & C) separated by D=4.36m at λ=2.2μm. (a) The incoherent image is multiplied by the interference term of equation 1 to obtain the coherent image. Zero tilt and OPD was assumed between the two telescopes. (b) and (c) show the effect on the coherent image of introducing an OPD = $\lambda/2$ (dashed curve) and a relative tilt (0.2 arcsec) between the two telescopes.

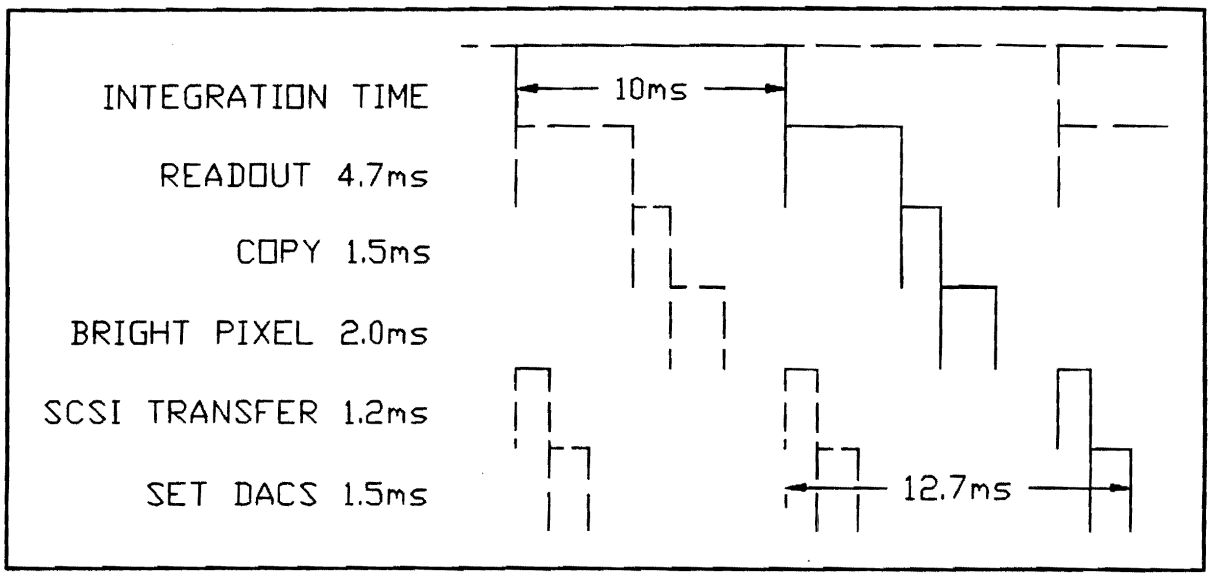

Figure 3. Timing diagram for real-time adaptive phasing of two MMT telescope.

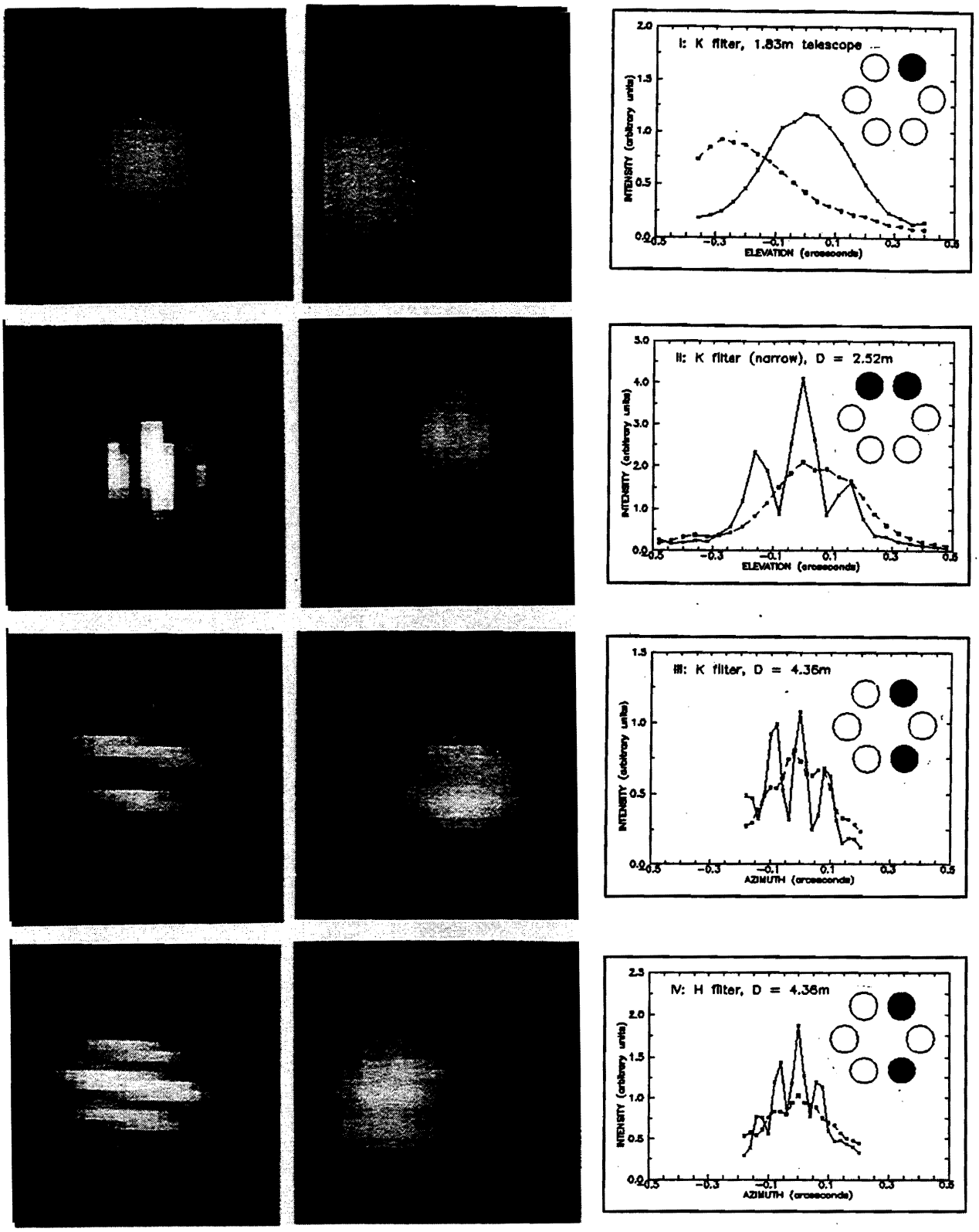

Figure 4. Integrated images (1000 coadded frames) with (left) and without (center) adaptive phasing/bright pixel tracking. The top image, I, is from a single telescope. Images II, III and IV are from the interference of two MMT telescopes. The intensity profile (right) is a cut perpendicular to the fringes. The parameters for each image are listed in Table 1.

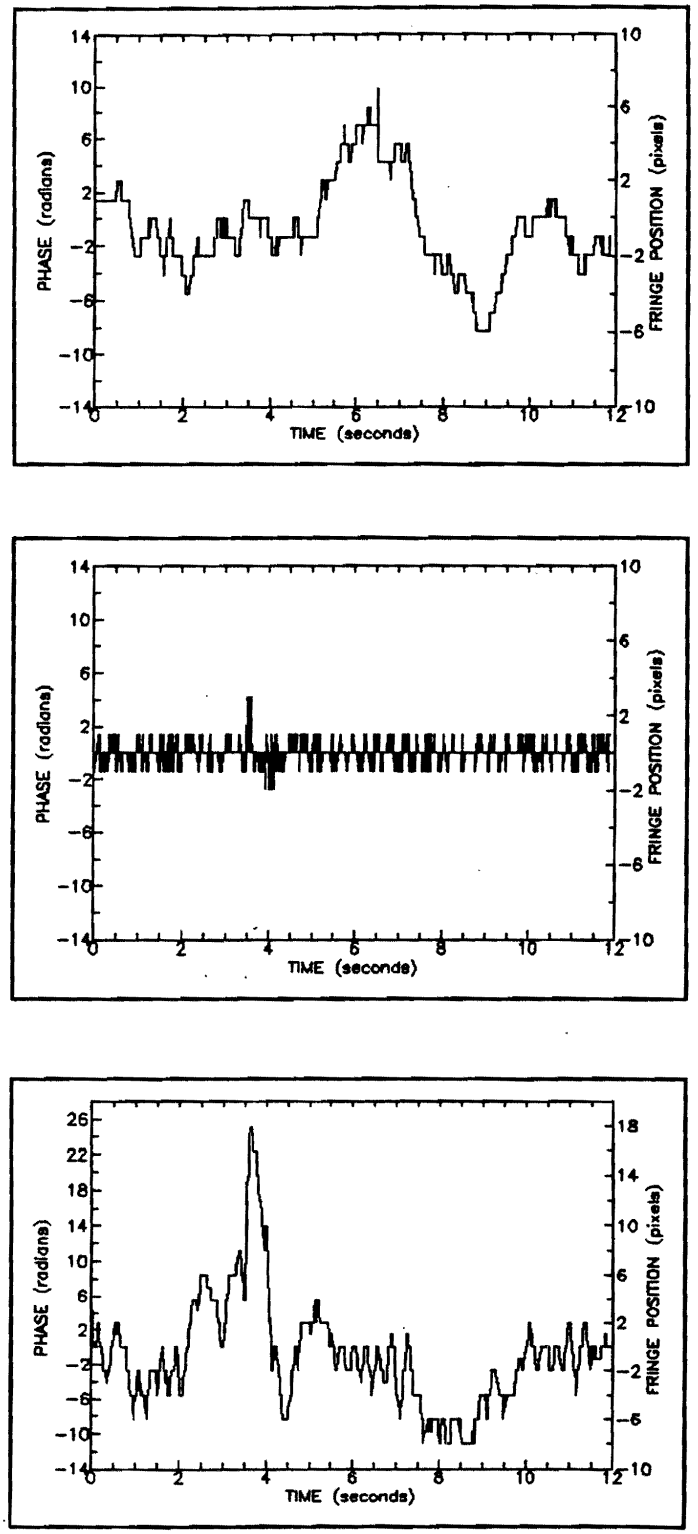

Figure 5. Temporal evolution of the phase difference between two MMT telescopes, as measured by the position of the brightest pixel on a given fringe, for image III of figure 4. The adaptive phasing system was off for the top plot and on for the other two plots. The bottom plot is the integration of the phase corrections made to obtain the middle plot.

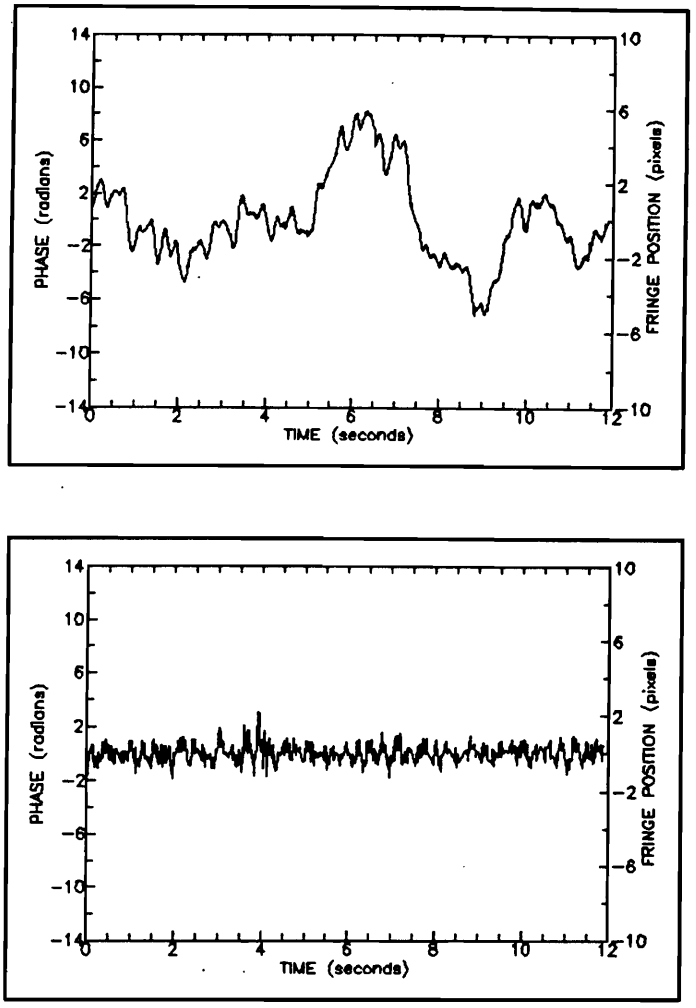

Figure 6. These plots are similar to the uncorrected and corrected phase plots of figure 5 except that a cosine function, instead of the brightest pixel location, was used to obtain a more accurate determination of phase.

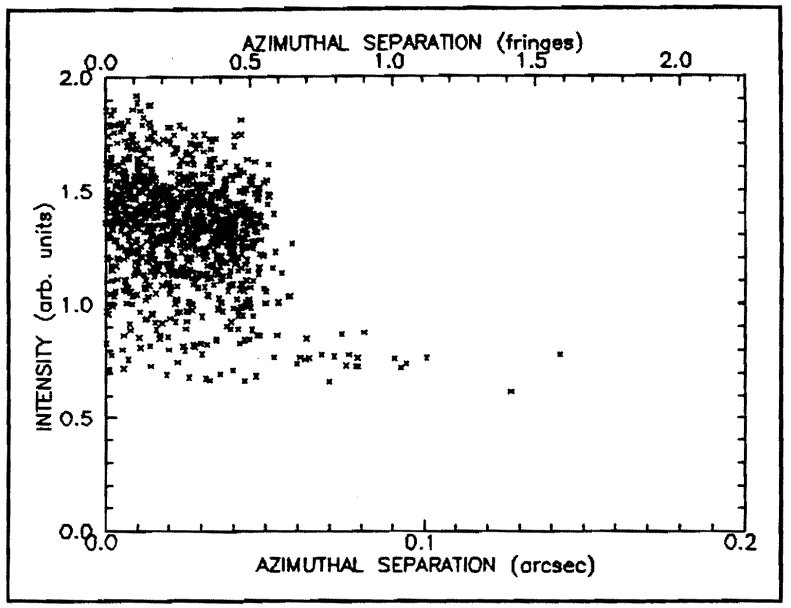

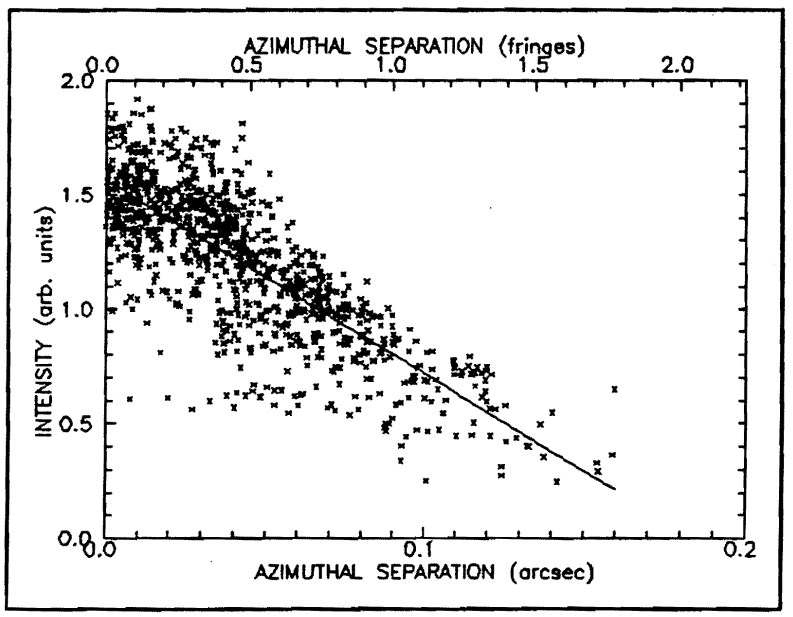

Figure 7. (a) Intensity of the brightest pixel of the corrected image set III as a function of the difference in azimuth between the centroid and bright pixel locations. (b) Same plot for the intensity and location of the brightest pixel within the central 6×6 pixel field (ie. on the tracked fringe).

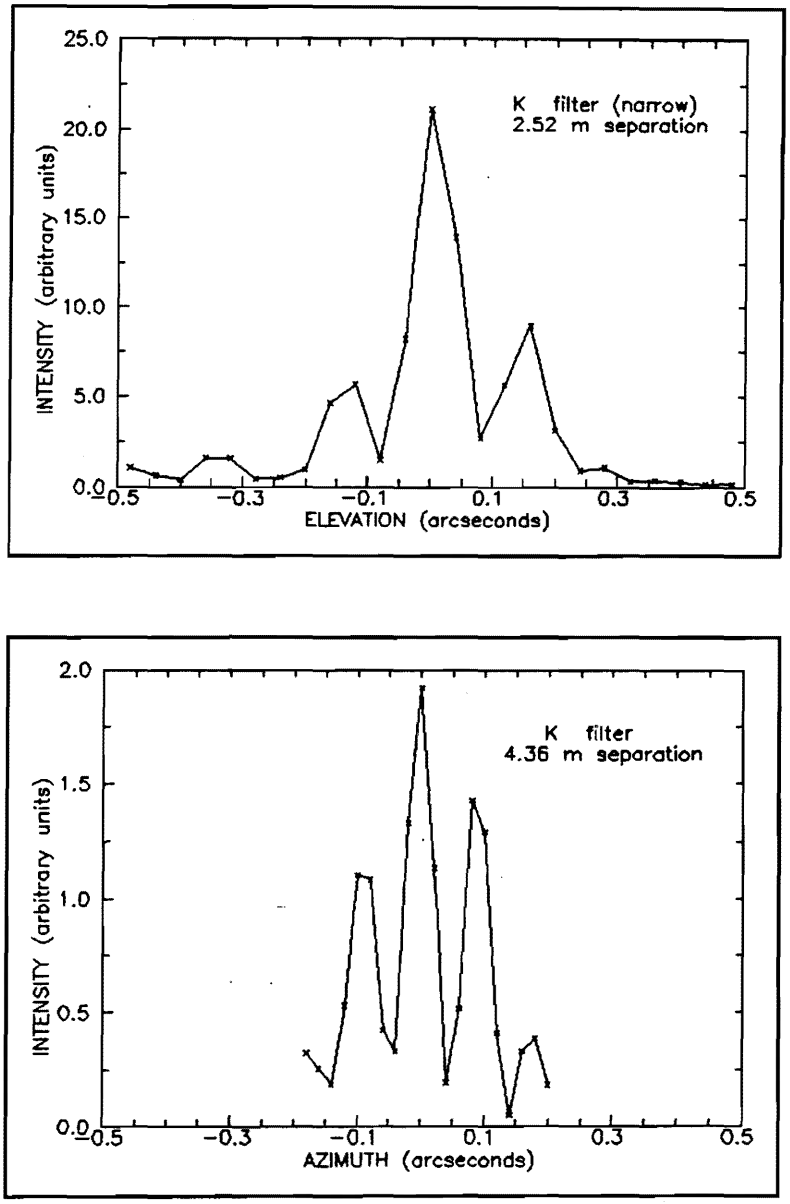

Figure 8. The best individual images, as judged by the brightest pixel intensity, from the data sets used to obtain the corrected integrated images II and III.

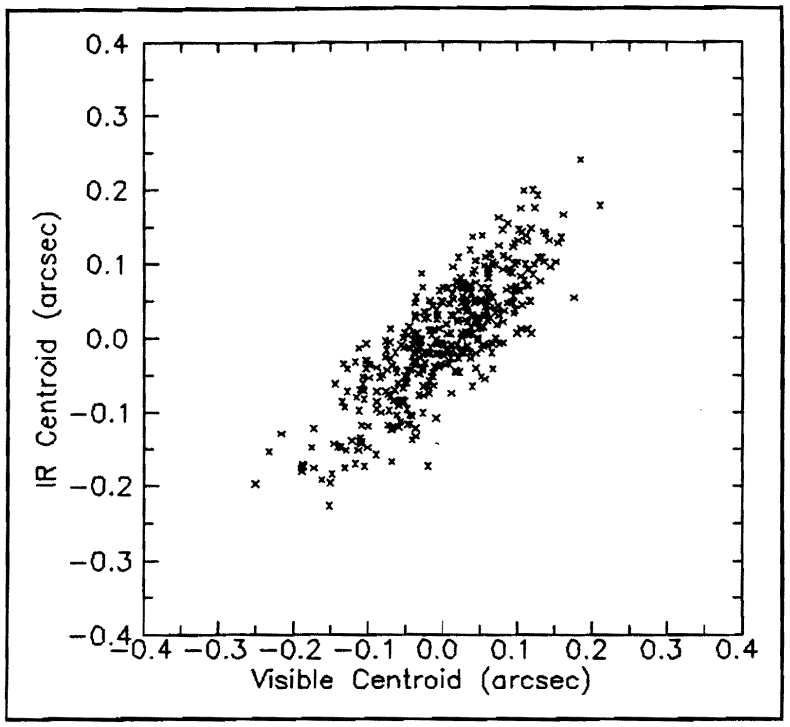

Figure 9. Infrared versus visible energy centroid for a single MMT telescope in azimuth.

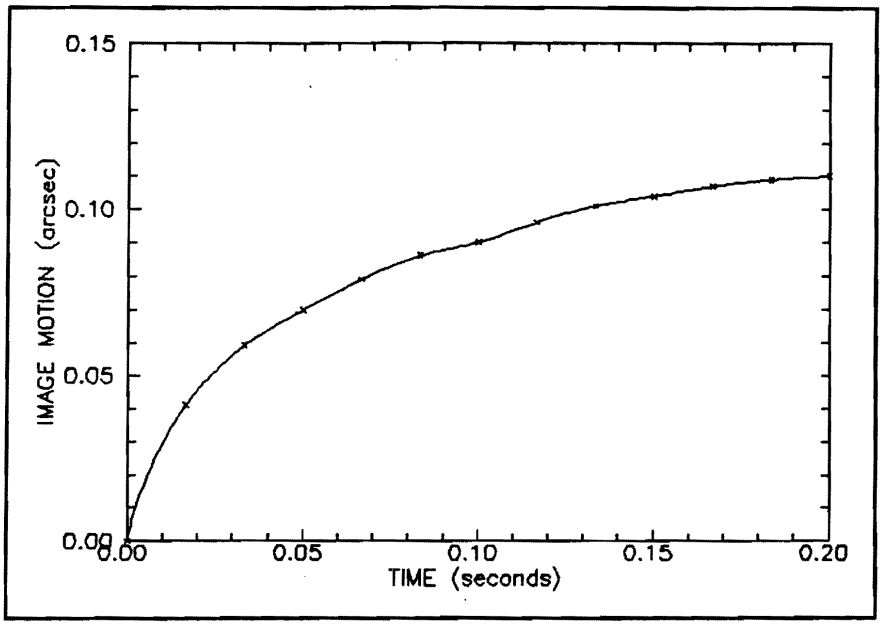

Figure 10. Average change in image position versus time for a single MMT telescope.